



# A seven-crystal spectrometer for high-energy resolution X-ray spectroscopy at Shanghai Synchrotron Radiation Facility

Bing-Bao Mei<sup>1</sup> · Liang-Xin Wang<sup>1</sup> · Song-Qi Gu<sup>1</sup> · Xiao-Zhi Su<sup>1</sup> · Shuo Zhang<sup>1</sup> · Yao Wei<sup>2</sup> · Jing-Yuan Ma<sup>1</sup> · Zheng Jiang<sup>3</sup> · Fei Song<sup>1</sup>

Received: 16 October 2023 / Revised: 10 January 2024 / Accepted: 11 January 2024 / Published online: 31 August 2024

© The Author(s), under exclusive licence to China Science Publishing & Media Ltd. (Science Press), Shanghai Institute of Applied Physics, the Chinese Academy of Sciences, Chinese Nuclear Society 2024

## Abstract

A Johann-type X-ray spectrometer was successfully developed at the hard X-ray branch (in-vacuum undulator with a 24-mm periodic length) of the energy material beamline (E-line) at the Shanghai Synchrotron Radiation Facility (SSRF). This spectrometer was utilized to implement X-ray emission spectroscopy (XES), high-energy resolution fluorescence-detected X-ray absorption spectroscopy (HERFD-XAS), and resonant inelastic X-ray scattering. Seven spherically bent crystals were positioned on the respective vertical 500-mm-diameter Rowland circles, adopting an area detector to increase the solid angle to 1.75% of  $4\pi$  sr, facilitating the study of low-concentrate systems under complex reaction conditions. Operated under the atmosphere pressure, the spectrometer covers the energy region from 3.5 to 18 keV, with the Bragg angle ranging from  $73^\circ$  to  $86^\circ$  during vertical scanning. It offers a promised energy resolution of sub-eV (XES) and super-eV (HERFD-XAS). Generally, these comprehensive core-level spectroscopy methods based on hard X-rays at the E-line with an extremely high photon flux can meet the crucial requirements of a green energy strategy. Moreover, they provide substantial support for scientific advances in fundamental research.

**Keywords** X-ray emission spectroscopy · High-energy-resolution X-ray spectrometer · Johann geometry · Energy materials · SSRF

This work was supported by the National Key Research and Development Program of China (Nos. 2022YFA1503801, 2021YFA1600800), the Photon Science Center for Carbon Neutrality of Chinese Academy of Sciences, Shanghai Science and Technology Development Funds (Nos. 22YF1454500, 23ZR1471400), the CAS Project for Young Scientists in Basic Research (No. YSBR-022), and the National Natural Science Foundation of China (No. 12305375).

✉ Song-Qi Gu  
gusq@sari.ac.cn

✉ Fei Song  
songf@sari.ac.cn

<sup>1</sup> Shanghai Synchrotron Radiation Facility, Shanghai Advanced Research Institute, Chinese Academy of Sciences, Shanghai 201800, China

<sup>2</sup> Shanghai Institute of Applied Physics, Chinese Academy of Sciences, Shanghai 201204, China

<sup>3</sup> National Synchrotron Radiation Laboratory, University of Science and Technology of China, Hefei 230026, China

## 1 Introduction

Determining the dynamic changes in the local atomic and electronic structures under real reaction conditions is essential for a deeper understanding of the structure-performance relationship of energy materials. Synchrotron radiation X-ray spectroscopy (SRXS) stands out as a powerful tool for tracing subtle molecular and atomic structures, including the absorption and desorption of intermediates. It is generally realized that SRXS can reveal contributions from the orbital and spin states, charge transfer, geometric symmetry, and coordination configurations [1–4]. However, certain characterization technologies are significantly restricted by their intrinsic limitations. For example, X-ray photoelectron spectroscopy (XPS) and electron energy loss spectroscopy (EELS) can only be implemented under ultrahigh vacuum, which substantially hinders their application under operando conditions [5]. Consequently, bridging the pressure gap, expanding the energy range of X-rays, and enriching spectroscopic measurements with a comprehensive characterization

platform can facilitate the acquisition of extensive atomic structures for energy materials in situ or operando environments [6, 7].

X-ray emission spectroscopy (XES) is recognized as the decay process following X-ray absorption owing to electron de-excitation from a higher energy level to the core hole. According to the Kramers-Heisenberg equation, the energy resolution of XES relies on the core hole lifetime of 2p/3p orbitals rather than that of the 1 s orbital, promising narrower broadening compared to conventional X-ray absorption fine structure (XAFS) [8, 9]. Consequently, XES can reveal subtle electronic structures, including charge transfer, spin state, and orbital hybridization, and can distinguish ligand types with similar scattering effects [10]. The  $K\beta'$  satellite of the main line lying in the lower-energy position is ascribed to the p-d exchange interactions that are sensitive to the spin state. Jaouen et al. identified the spin state of Fe-N-C catalysts induced by external potentials under the oxygen reduction reaction (ORR) by monitoring the intensity changes of the  $K\beta'$  peak [2, 3]. While Mössbauer spectroscopy is considered to be the fingerprint of electronic structures, its detection limit is restricted to several elements, significantly hindering its general applications [11]. In contrast, valence-to-core XES (VtC-XES), which involves the transmission of ligand orbital contributions to the core level of the center atoms, is sensitive to fine electronic states and ligand types. Consequently, VtC-XES has garnered significant attention in the fields of catalytic chemistry, material science, environmental science, and other fields [12]. DeBeer et al. employed Fe  $K\beta''$  XES to clearly identify the active center in the nitrogenase iron-molybdenum cofactor as  $C^{4-}$ , instead of  $N^{3-}$  or  $O^{2-}$  in combination with theoretical calculations, breaking the limitation that the scattering of C, N, and O atoms is unrecognizable via conventional XAFS [13].

In the total fluorescence yield mode, routine XAFS is usually performed using Lytle or silicon drift detectors (SDD) with an energy resolution of less than 100 eV. This approach involves the collection of nearly all fluorescence lines, including  $K\alpha$  and  $K\beta$  emission lines, as well as undesired noise from the supports and elastic scattering. As a consequence, the resulting spectrum often exhibits poor energy resolution, with fine features buried. In high-energy-resolution fluorescence-detected X-ray absorption spectroscopy (HERFD-XAS), only the desired emission line is detected by the high-energy-resolution spectrometer, making it a powerful tool for investigating elaborate atomic and electronic structures. For example, the dynamic structural changes in copper(II) phthalocyanine during the  $CO_2$  electrochemical reduction reaction can be determined through  $K\alpha_1$ -HERFD-XAS measurements. By eliminating elastic scattering and other uninteresting fluorescence lines, the pre-edge, shoulder, and multiple scattering features are enlarged

in HERFD-XAS, making further data processing convenient [14]. In addition, difference spectroscopy ( $\Delta\mu$ ) analysis was also developed for X-ray absorption by subtracting the initial spectrum from that in the reaction condition; therefore, only the changed state from the active/metal center was obtained. Nevertheless, the subtraction between the two spectra results in the  $\Delta\mu$  features being weaker; however, the intense features in HERFD-XAS can ensure the quality of  $\Delta\mu$  data [15, 16]. To this end, HERFD-XAS measurement combined with the  $\Delta\mu$  analysis technique is a conclusive tool for obtaining important pieces of information on the chemical nature of in situ reactions.

In general, high-energy-resolution X-ray spectroscopy spectrometers are classified into von Hamos and Johann types, which utilize cylindrical and spherical analyzer crystals, respectively, [17–19]. Without moving the crystal or detector for energy scanning, the von Hamos-type spectrometer can obtain the entire spectrum over a wide energy range. However, the small solid angle, and thus the weak signal/noise ratio, prevents its application in dilute samples or operando measurements. Based on a high-flux light source and multiple crystals, the von Hamos spectrometer is appropriate for time-resolved XES measurements. Given that the solid angle of the Johann-type X-ray spectrometer is approximately 1000 higher than that of the von Hamos type, complex materials with interfacial structures, dilute contents, or rigorous reaction conditions can be precisely measured using a Johann-type spectrometer. Several Johann-type X-ray spectrometers have been developed for synchrotron facility. Gao et al. developed a single-crystal spectrometer at the BL14W1-XAFS beamline of SSRF with the crystal radii of 182 and 1000 mm to study radionuclides and 3d transition metals, respectively, [20]. Based on this, Duan et al. utilized three crystals with a curvature radius of 1000 mm to improve the solid angle from 0.6% to 1.87 % of the total four  $\pi$  sr values placed on the corresponding Rowland circles in an X-ray spectrometer [21–23]. Five- and seven-crystal Johann-type X-ray spectrometers were installed in the SuperXAS beamline at the Swiss Light Source and in beamline 6–2 at the Stanford Synchrotron Radiation Light Source, respectively [24, 25].

In this context, we report a Johann-type spectrometer equipped with seven bent crystals developed in the hard X-ray branch of the E line at SSRF. In the field of energy materials, spectrometers play a crucial role in operando/in situ high-energy-resolution X-ray spectroscopy. This technique is employed to precisely explore the local configuration changes of active sites, which determine the intrinsic performance of catalytic reactions. Detailed descriptions of the geometric parameters, orientation, and operational regulation modes are presented. Moreover, an in situ high-energy resolution experiment was conducted to verify the performance of the spectrometer.

## 2 Hard X-ray branch of the E-line

Based on the SSRF which is a third-generation light source with a 3.5 GeV storage ring and 200 mA beam current, a hard X-ray branch of the E-line with a photon flux of  $2 \times 10^{12}$  photons/s (0.1%BW) at 5 keV and a beam size of  $80 \mu\text{m} \times 20 \mu\text{m}$  was constructed using 24-pole in-vacuum undulators [26–30]. The E-line covers a wide energy range from 130 eV to 18 keV and offers a comprehensive spectroscopy characterization platform that meets the major needs of the green energy strategy to support users from related fields in contributing significant scientific advances [31, 32]. The experimental station of the hard X-ray branch constitutes a multidisciplinary platform with an independent work hutch. The center of the experimental station was 45.6 m away from the light source. The hard X-ray branch is mainly employed to study the electronic and local structures of active atoms and ions in the bulk phase of energy materials, and is thus complementary to the soft X-ray branch and the combined soft-hard X-ray branch of the E-line in terms of spectroscopy techniques. The hard X-ray branch is highly significant for the entire beamline and is designed to address the characterization challenges and limitations for an in-depth understanding of energy materials. Focusing mirrors, slits, and harmonic suppression mirrors are considered as constraints in the optical path to meet the intricate design requirements. The monochromator was equipped with two crystals (Si(111) and Si(311)) that provided a monochromatic beam from 2.3 to 18.0 keV. Although Si(111) can cover the entire energy range, the Si(311) mode is used to achieve high-energy resolution because of its sharp rocking curve on a high-index silicon surface. The two sets of crystals were installed inside the monochromator for easy switching. Monochromator performance and crystal deformation have been proven to meet the requirements of the stability and spot size of the beam at the end station. In addition to considering the energy region and energy resolution, an important factor in the selection of silicon crystals is that the thermal expansion coefficient near 125 K is close to zero with a relatively large heat-transfer coefficient, which is beneficial for cooling with liquid nitrogen [33].

In addition to high-energy resolution X-ray spectroscopy methods, X-ray Raman spectroscopy (XRS) has also been developed to investigate the K-edge absorption of 2p elements, including C, N, and O, and the L-edge XAS of 3d transition elements, consequently surpassing the limitations of the probing depth and vacuum condition from typical soft X-ray absorption measurements. The XRS spectrometer comprises a sample stage, an array of 25 analyze crystals, and a detector system located on a Rowland circle geometry. These crystals were placed along the optical

path behind the sample point, primarily capturing the low-q portion of the signal. A large marble load-bearing motion platform was used to host the entire system (e.g., the seven-crystal spectrometer, 25-crystal XRS spectrometer, and detector), which can move along both the horizontal and vertical directions and ensure the relative position relationship among these devices. Thus, the experimental efficiency is effectively improved. Furthermore, slide rails were set under this large platform to accommodate a wider range of the X-Y direction movements.

In other words, the hard X-ray branch design was optimized in terms of the energy range, photon flux, energy resolution, and operando conditions to meet the crucial requirements of the applied research field. An in situ SRXS measurement can be conducted under rigorous conditions, including a temperature limit and high pressure. The operation of the E-line is of significant importance for addressing the challenge of in situ characterization limitations and promoting an in-depth study of the structure–property relationship of energy materials.

## 3 Spectrometer design

The Bragg angle in the Johann-type geometry was determined by the relative position of the sample using a spherically bent crystal analyzer (SBCA) with a curvature radius of  $2R$  and a detector placed on a Rowland circle with a radius of  $R$ . The entire XES spectrum based on point-to-point scanning was obtained by the simultaneous motion of SBCA and the detector, with the sample fixed to vary the Bragg angle. Scanning is generally divided into rotational and translational modes, based on the orientation adjustment of SBCA (Fig. 1). In the former case, the rotation angle of SBCA was adjusted to scan the Bragg angle while simultaneously being moved along the line connecting the sample and the crystal center to match the Rowland circle. Lacking a linear relationship between the SBCA and detector movements, the signal collected by the detector could not properly converge to the actual position of the fluorescence spot, resulting in decreased energy resolution and count rate. Consequently, a considerably accurate initial position with a Bragg angle of  $90^\circ$  was required, which could hardly be achieved, and the spectrometer introduced an additional high degree of debugging. In translational mode, the SBCA was moved straight in two perpendicular directions, and the detector was translated along only one of these two directions. Thus, the experimental data obtained in translational acquisition mode are more accurate. The crystal, sample, and detector were consistently positioned within the Rowland circle, a configuration that reduced the experimental error and improved the energy resolution. Moreover, the target fluorescence spot on the detector was always focused on the Rowland circle,

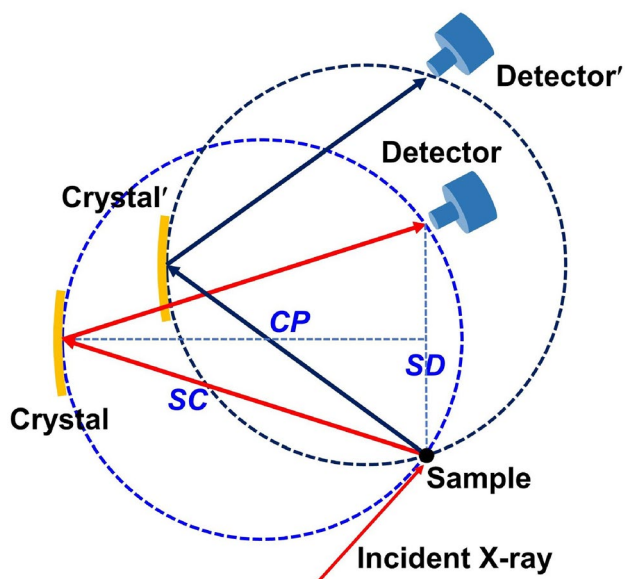


**Fig. 1** (Color online) Schematic representation of the Johann-type X-ray emission spectrometer working under the translational modes. The curvature radius of Rowland circle (dashed) is 250 mm

thereby improving the count rate and promoting a higher signal-to-noise ratio.

Arranging on the Rowland circle with the midpoint between the sample and detector aligned, seven identical SBCAs were used to increase the signal collection efficiency (Fig. 2a). Each of the seven crystals was arranged on an individual vertical Rowland circle, sharing the same sample point and detector. The slight vertical divergence of the incident X-ray beam was also considered in this arrangement, promoting an improvement in the energy resolution. Considering the space limitations and motion range of the motors, the individual regulation stages of the crystal analyzers were set to 16° with respect to each other (Fig. 1b). The spectrometer was operated in the translational mode, considering the tedious orientation adjustment of the seven crystals. The relative positions of the key elements in the spectrometer, namely, the distance between the crystal and the sample (SC), the distance between the sample and the detector (SD), and the projected distance from the crystal to the sample-detector plane (CP), were calculated as follows based on the Bragg equation:

$$SC = 2R \cdot \sin \theta, \tag{1}$$

$$SD = 4R \cdot \sin \theta \cdot \cos \theta, \tag{2}$$

$$CP = 2R \cdot \sin^2 \theta, \tag{3}$$

where  $\theta$  denotes Bragg angle.

The XES spectrum was obtained by scanning the Bragg angle and regulating the relative positions of the crystals,

detector, and sample. The SC, SD, and CP values varied during scanning. Accordingly, all seven crystals could move upward through the high-torque motor and forward through the individual step motors. Three additional degrees of freedom (i.e., goniometer, rotation, and Z stage) were added to each crystal to guarantee focusing on the same point.

The Bragg angle range covered by the spectrometer was determined based on the geometric size and motion range. The maximum Bragg angle was determined by the minimum distance between the sample and detector, as exceeding this distance risked collision between the detector and the sample. Consequently, the Bragg angle hardly reached 90° due to the space limitations. Conversely, the minimum Bragg angle is related to the limited position of the Y motor because the height of the detector can be further increased by installing an additional lifting platform. Consequently, the Bragg angle range was obtained using the following equation:

$$\theta_{MAX} = 90^\circ - \frac{1}{2} \cdot \arcsin \left( \frac{SD_{MIN}}{2R} \right), \tag{4}$$

$$\theta_{MIN} = \arcsin \sqrt{\frac{CP_{MIN}}{2R}}. \tag{5}$$

Moreover, the energy range of the spectrometer was determined by both the limit positions of the motors and the crystal curvature radius. These crystal wafers with a diameter of 100 mm were bent into a spherical surface with a curvature radius of 500 mm. Notably, crystal analyzers were used to release stress and reduce Darwin broadening to improve the energy resolution. The entire spectrum from the  $K\beta$  main line to the VtC-XES was measured by loading crystals with optimal Miller indices, which facilitated further data processing by subtracting the high-energy tail [9].  $SD_{MIN}$  and  $CP_{MIN}$  of the XES spectrometer in the E-line were approximately 70 mm and 457 mm, respectively, corresponding to the Bragg angle ranging from 73° to 86°. The appropriate energy range covered by the crystal analyzers in the spectrometer was determined as follows:

$$E = \frac{12398.5}{2d \cdot \sin \theta}, \tag{6}$$

where  $d$  is the crystalline interplanar spacing determined by the Miller indices and tabulated lattice parameters.  $d$  for the Si and Ge crystals was calculated using Eqs. (7) and (8), respectively.

$$d_{Si} = \frac{5.4309}{\sqrt{h^2 + k^2 + l^2}} \tag{7}$$

$$d_{Ge} = \frac{5.6574}{\sqrt{h^2 + k^2 + l^2}} \tag{8}$$

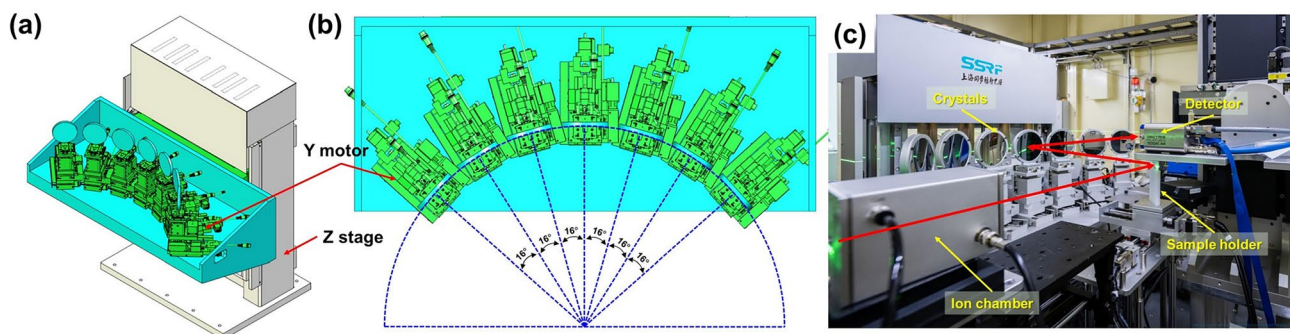


**Fig. 2** (Color online) Mechanical drawing of the crystal motion control system in **a** isometric projection and **b** top view. **c** Photograph of the seven-crystal Johann-type spectrometer settled in the E-line

The minimum and maximum energies reached by a silicon crystal with special indices  $h_0$ ,  $k_0$ , and  $l_0$  can be deduced and simplified as follows:

$$E_{\text{MIN}} = 1144.26 \cdot \sqrt{h_0^2 + k_0^2 + l_0^2} \quad (9)$$

$$E_{\text{MAX}} = 1193.63 \cdot \sqrt{h_0^2 + k_0^2 + l_0^2} \quad (10)$$

The corresponding energies for the germanium crystals with identical indices were determined as follows:

$$E_{\text{MIN}} = 1098.45 \cdot \sqrt{h_0^2 + k_0^2 + l_0^2} \quad (11)$$

$$E_{\text{MAX}} = 1145.84 \cdot \sqrt{h_0^2 + k_0^2 + l_0^2} \quad (12)$$

The overlap in the energy ranges of Ge and Si crystals with identical Miller indices suggests that these two types of crystals are suitable for covering the energy range of 3.5–18 keV. For example, the  $E_{\text{min}}$  of Si(220) is 3.2 keV, the  $E_{\text{min}}$  of Si(440) is 6.4 keV, and the Si(220) in 6th order is 19.2 keV. Similarly, the general indices of Si and Ge cover the emission lines from most of the elements of interest.

In the setup of spectrometer, two detectors were installed to collect the selected X-ray fluorescence: a four-element SDD from Vortex and a position-sensitive detector (PSD) from PILATUS 100K. While charge-coupled devices are often used to record X-ray images, an additional shutter must be installed on the incident path to suppress dark current and readout noise. Furthermore, the relatively poor conversion efficiency of photons to signals (i.e., approximately 50%) hinders the collection of abundant emission lines at synchrotron radiation facilities. PSD is generally utilized in point-to-point spectrometers, which require a short readout time, high single-to-noise ratio, and a wide energy range. As a hybrid pixel detector, PILATUS 100K with direct deposition of X-ray photons in a readout chip

avoids secondary conversion and increases the counting rate, making it suitable for high-flux stations [34, 35]. The good detective quantum efficiency of high-energy photons ensures a wide energy range of 3.5 to 18 keV, using only silicon sensor instead of GeTe or GaAs. With an energy resolution of approximately 1000 eV, the threshold can be set to subtract undesired low-energy photons to improve the single-to-noise ratio. A large active area of 83.8 mm × 33.5 mm is also preferred for optimizing the spectrometer's orientation. Based on the merit of approximately 130 eV energy resolution, the SDD can restrain stray photon collection and further improve the spectrometer's energy resolution. By setting the rational energy threshold for the PSD to approximately half the target energy, the undesired scattering distance is generally hindered. Unlike the von Hamos-type spectrometer, the PSD is used only for counting, instead of position-sensitive recording. The 172 μm × 172 μm pixel size of PILATUS 100K is sufficiently small for high-energy resolution spectroscopy measurements, even though it is larger than the beam spot (80 μm × 20 μm).

Although incident X-rays are primarily utilized to excite core-level electrons, the precise energy set is crucial, extending beyond mere surpassing of the absorption edge. Multiple excitations should be considered because they result in an additional undesired satellite  $K\beta_{2,5}$  peak at the high-energy tail of the  $K\beta_{2,5}$  peak. This phenomenon poses challenges in signal normalization and background subtraction [36]. The highest energy of the incident X-rays should not exceed the sum of the binding energies of the 1s and 2p orbitals of Z and Z + 1, respectively. For example, it will be best to set the incident energy below 7383.6 eV during the XES measurement of Mn species, calculated from the K-edge energy of Mn (6539 eV) plus the L-edge energy of Fe (844.6 eV). In an undulator beamline, the photon flux is strongly dependent on the gap and taper of the poles [37]. During the XES measurements, the incident energy was fixed, and the taper was set to zero to ensure the incident flux was at the harmonic peak. For HERFD-XAS and RIXS measurements, an

**Fig. 3** (Color online) **a** Schematic view of the XES measurement of the sample with  $\delta x$  thickness variation. **b** The  $K\beta$  main line of  $MnCl_2$  with the sample loading of 17 and 5 mg and Bragg angle scanned from  $83.7^\circ$  to  $86.2^\circ$

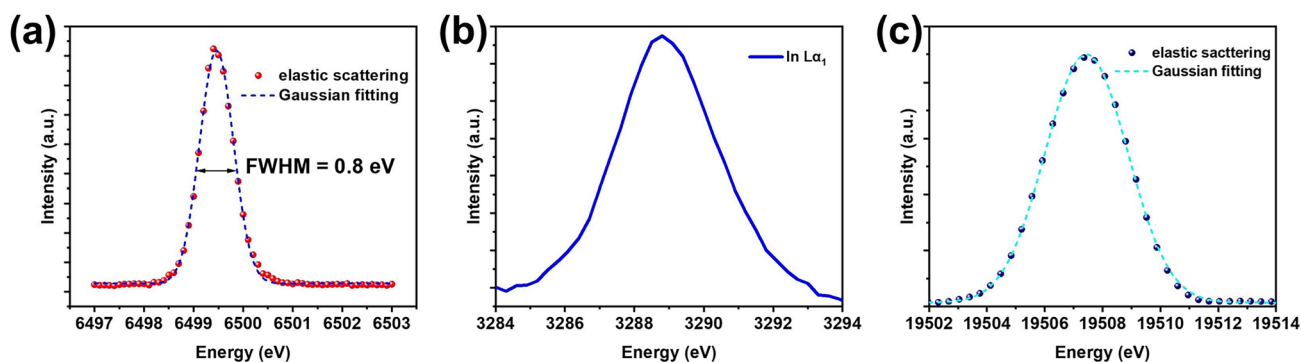
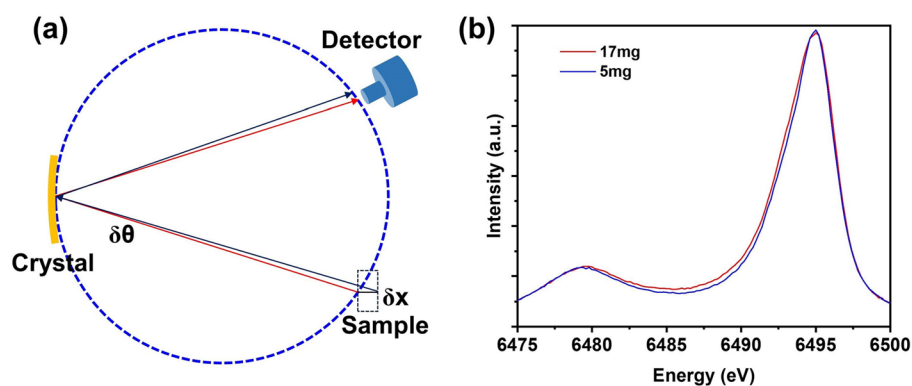


**Fig. 4** (Color online) **a** The elastic scattering peak and corresponding Gaussian fitting at 6499.5 eV; **b**  $In L\alpha_1$  X-ray emission spectrum based on the  $Si(220)$  crystals at the Bragg angle of  $79.1^\circ$ ; **c** the elastic

scattering peak at 19,507.5 eV based on the  $Si(220)$  crystals with the 6th order at the Bragg angle of  $83.5^\circ$

appropriate taper should be set to avoid a sharp decrease in flux in the XANES range. The incident X-ray intensity was recorded to normalize the XES spectra. An ion chamber was installed on an X-ray emission spectrometer. Gas inflation was controlled using automatic mixture equipment based on X-ray energy (Fig. 2c).

In addition to the intrinsic influence of the beamline and spectrometer on the energy resolution, the contribution of the sample (mainly the thickness) was also visible in the spectrum width. The thickness distorts the XES spectrum by changing the effective source point of emission. Assuming a sample thickness of  $\delta x$ , the difference in the emission points can result in a deviation in the Bragg angle  $\delta\theta$  (Fig. 3a). The relationship between these two parameters was calculated as follows:

$$\delta\theta = \frac{\delta x}{2R \cdot \tan\theta}. \quad (13)$$

Correspondingly, energy offset can cause spectral broadening (Eq. (14)):

$$\delta E = \frac{12398.5}{4d \cdot R} \cdot \frac{\cos^2\theta}{\sin^3\theta} \cdot \delta x. \quad (14)$$

Based on this, loading an excess sample volume into the tablet is not reasonable, even though the emission count is increased. Hence, the balance between the fluorescence quantum efficiency and spectral broadening should be considered during sample preparation. For example,  $MnCl_2$  powders with loading contents of 5 and 17 mg were pressed into tablets to directly verify the influence of the sample thickness on the broadening of the XES spectrum (Fig. 3b). The  $K\beta_{1,3}$  peak of the 17 mg tablet clearly exhibits a wider peak with a full width at half maximum (FWHM) of 0.3 eV compared to that of the 5 mg tablet. Moreover, the thickness effect can result in errors during the quantitative analysis of the peak intensity. Thus, identical sample contents should be loaded into the tablet to avoid undesired spectral broadening during measurements. To achieve uniform sample thickness, holders with a fixed thickness of several hundreds of microns can be used to pack the fine-ground sample powder, and thin Kapton tape can be used to seal the sample.

In addition, elastic scattering at 6499.5 eV using a  $Si(440)$  crystal was performed to demonstrate the energy resolution of the spectrometer. Figure 4a illustrates the peak with a FWHM of 0.8 eV, which was considerably lower than the core-hole lifetime broadening of emission lines of most heavy elements. This result clearly demonstrates the

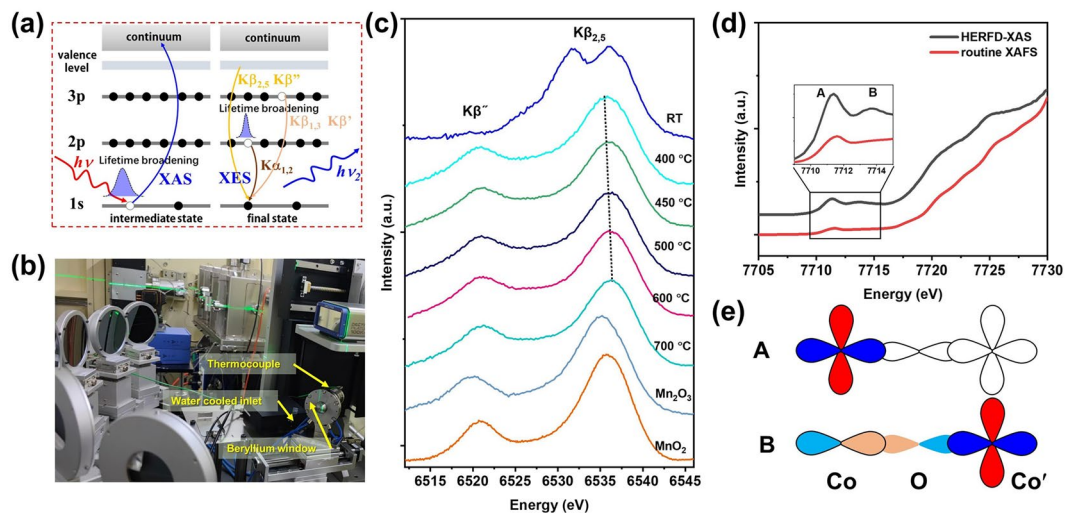


**Fig. 5** (Color online) **a** The schematic diagram of transitions; **b** photograph of the in situ XES measurement with a thermal cell; **c** VtC-XES spectra of  $\text{MnCO}_3$  during pyrolysis; **d**  $\text{Co}_2\text{O}_3$ -HERFD-XAS and

routine XAFS of  $\text{Co}_2\text{O}_3$ ; and **e** the final-state configurations of local  $1s^13d^8$  quadrupole (A) transitions and non-local  $1s^13d^74p(3d^8)$  dipole transitions (B)

excellent capacity of the XES spectrometer to determine imperceptible electronic dynamics [38, 39]. Furthermore, the energy range covered by the spectrometer determined the targets of the elements of interest. In this study, the  $\text{In } L\alpha_1$  emission spectrum was obtained using  $\text{Si}(220)$  crystals. Figure 4b, whereas the emission line at approximately 3289 eV was efficiently collected by tuning the Bragg angle to  $79.1^\circ$  with a helium bag. The extremely low energy limit promotes the investigation of L-edge XES of 4d transition elements and M-edge XES of actinium series elements. Elastic scattering at 19,507.5 eV was obtained using the same crystals, demonstrating the capacity to measure partial 4d/5d transition elements and uranium-series elements (Fig. 4c).

## 4 Experiments

By utilizing seven  $\text{Si}(440)$  crystals and the PILATUS 100K PSD, the local electronic structure changes of  $\text{MnCO}_3$  pyrolysis under ambient atmosphere were investigated through in situ VtC-XES. The incident X-ray energy was 7.0 keV with a flux of  $\sim 10^{12}$  photons/s. Considering the influence of attenuation in air, transition probability, and elemental content, the counts reaching each crystal were  $\sim 10^5$  photons/s. In the experiment, the Bragg angle was scanned at approximately  $81.52^\circ$ , indicating that the selected fluorescence X-ray could travel in the air for 1 m and that the transmission fraction was less than 10%. A helium bag was fixed between the crystals and the detector, especially for VtC-XES collection, as the intensity was approximately two orders of magnitude weaker than that of the  $K\beta$  main line (Fig. 5a). A proper counting area is crucial for high-energy resolution

because the energy of photons recorded within broad pixels can be shifted by aberrations; therefore, no more than 10 rows of pixels were selected. In addition, an in situ thermal cell was specially designed for the XES measurements (Fig. 5b). The beryllium window was curved to the hemisphere to maximize the exit angle and maximize the collection of signals from the seven crystals. The distance from the center of the detector to the top edge of the sample holder was shorter than  $SD_{\text{MIN}}$  of 70 mm, while ensuring a reasonable layout for the gas and cool water pipelines. The energy step for the in situ measurement was set to 0.2 eV. The integration time was set as 10 s. The  $\text{MnCO}_3$  solid was ground into a fine powder, which was then pressed into tablets.

As the temperature increased from room temperature to  $400^\circ\text{C}$ ,  $\text{MnCO}_3$  dissociated rapidly along with the release of  $\text{CO}_2$  and evolved into oxides, as evidenced by the appearance of the  $K\beta_{2,5}$  peak at 6532 eV (Fig. 5c). With a further increase in temperature, the  $K\beta''$  peak at 6520 eV arising from the ligands' 2s to the metal's 1s transition gradually shifts by approximately 0.7 eV. The same shift was observed for the  $K\beta_{2,5}$  peak. As illustrated in Fig. 5a, the position difference from the  $K\beta_{2,5}$  peak to the  $K\beta''$  peak is determined by the energy level difference between the ligands' 2s and 2p orbitals. Kwon et al. reported that the peak position of  $K\beta_{2,5}$  mainly depends on the valence state of the Mn species [40]. Compared with the reports on  $\text{Mn}_2\text{O}_3$  and  $\text{MnO}_2$  in the literature, the Mn species in  $\text{MnCO}_3$  were oxidized to  $\text{Mn}^{3+}$  and  $\text{Mn}^{4+}$  at extremely high temperatures. Thus, this demonstration experiment verified the in situ capability of XES measurements under rigorous conditions.

HERFD-XAS was performed with the emission energy fixed by scanning the incident energy and tuning

a double-crystal monochromator [41]. HERFD-XAS was generally collected at the  $K\beta_{1,3}$  main line because the peak broadening of the  $K\alpha$  line was extremely large and the emission energy of  $K\beta_{2,5}$  was close to the incident energy, which could lead to elastic scattering. During the HERFD-XAS measurements, the  $K\beta_{1,3}$  XES spectrum was collected to determine the peak position and calibrate the energy position to the corresponding emission line. To ensure background subtraction, the starting energy must be at a minimum of 20 eV lower than the absorption edge. During the ex situ measurement, the sample was pressed into a tablet and within a specialized holder matching the clamp to reduce the degrees of freedom and maintain constant emission energy. As a representative stable bulk oxide,  $\text{Co}_2\text{O}_3$  is typically used as a reference to demonstrate its valence state and coordination configuration. Thus, determining the accurate origin of fine structures is vital for investigating the characteristics of the materials of interest [42]. In this study, HERFD-XAS of  $\text{Co}_2\text{O}_3$  was conducted. Figure 5d compares the HERFD-XAS and routine XAS of  $\text{Co}_2\text{O}_3$ . The pre-edge feature in HERFD-XAS was more intense, and the second pre-edge peak was clearly resolved, further implying that HERFD-XAS is a powerful tool for investigating weak features in the pre-edge region.  $\text{Co}_2\text{O}_3$  is a typical low-spin oxide with a fulfilled  $t_{2g}$  orbital and an empty  $e_g$  orbital corresponding to the first pre-edge peak at 7711.4 eV ( $3d^7 \rightarrow 1s^1 3d^8$  transition). In contrast, the second pre-edge peak at 7713.7 eV originated from the delocalized transition from 1s to the mixing orbital of the local 4p and 3d of the neighboring Co atom bridged with oxygen (Fig. 5e) [43, 44].

## 5 Conclusion

As is commonly known, a thorough comprehensive of the reaction mechanisms occurring at the catalyst surface/interface is essential for the informed design of novel, cost-efficient, and stable catalysts, given that the majority of reactions take place at these locations. Traditional hard X-ray spectroscopy can be used to obtain bulk-averaged structural information straightforwardly owing to its strong penetrating depth. Although soft or tender X-ray spectroscopy is more surface sensitive, operando measurements are hindered by vacuum conditions. Toward this end, high-energy-resolution SRXS technology combined with operando/in situ measurements offers a conclusive tool for obtaining valuable information on the chemical nature of catalysts.

The development of a seven-crystal Johann-type X-ray spectrometer with a high-energy resolution at the E-line in SSRF is discussed in detail herein. Covering a wide Bragg angle range from  $73^\circ$  to  $86^\circ$ , the spectrometer can detect emission lines from 3.2 to 19.5 keV with appropriate Si or Ge crystals, which can meet most demands from both

fundamental and applied research fields. The sub-eV energy resolution benefits the accurate detection of fine electronic structures under in situ or operando conditions, including charge transfer, orbital splitting, and electron spin states. A large solid angle ensures that dilute samples or weak transition probability emission lines can be detected with a reasonable single-to-noise ratio. A spectrometer operating at the E-line will promote a deep investigation of the relationship between dynamic electronic structures and activity, further guiding the rational design of high-performance and long-term stability catalysts.

**Acknowledgements** Collaboration with Dr. Fei Zhan is greatly appreciated during the construction of spectrometer.

**Author contributions** All authors contributed to the study conception and design. Material preparation, data collection and analysis were performed by Bing-Bao Mei, Liang-Xin Wang, Fei Song and Song-Qi Gu. The first draft of the manuscript was written by Bing-Bao Mei and all authors commented on previous versions of the manuscript. All authors read and approved the final manuscript.

**Data availability statement** The data that support the findings of this study are openly available in Science Data Bank at <https://cstr.cn/31253.11.sciencedb.j00186.00532> and <https://www.doi.org/10.57760/sciencedb.j00186.00532>.

## Declarations

**Conflict of interest** The authors declare that they have no Conflict of interest.

## References

1. Y.-P. Liu, L. Yao, B.-J. Wang et al., Silicon PIN photodiode applied to acquire high-frequency sampling XAFS spectra. *Nucl. Sci. Tech.* **33**, 91 (2022). <https://doi.org/10.1007/s41365-022-01066-2>
2. V.A. Saveleva, K. Ebner, L. Ni et al., Potential-induced spin changes in Fe/N/C electrocatalysts assessed by in Situ X-ray emission spectroscopy. *Angew. Chem. Int. Ed.* **60**, 11707–11712 (2021). <https://doi.org/10.1002/anie.202016951>
3. J. Li, M.T. Sougrati, A. Zitolo et al., Identification of durable and non-durable FeNx sites in Fe–N–C materials for proton exchange membrane fuel cells. *Nat. Catal.* **4**, 10–19 (2021). <https://doi.org/10.1038/s41929-020-00545-2>
4. Y. Zou, H. Xu, G. Wu et al., Structural analysis of  $[\text{ChCl}][\text{m}[\text{ZnCl}_2]\text{n}]$  ionic liquid by X-ray absorption fine structure spectroscopy. *J. Phys. Chem. B* **113**, 2066–2070 (2009). <https://doi.org/10.1021/jp809788u>
5. P. Amann, B. Klötzer, D. Degerman et al., The state of zinc in methanol synthesis over a Zn/ZnO/Cu(211) model catalyst. *Science* **376**, 603–608 (2022). <https://doi.org/10.1126/science.abj7747>
6. H. Zhang, L. Xie, Z.-F. Liang et al., Tandem catalysis for enhanced CO oxidation over the Bi–Au–SiO<sub>2</sub> interface. *Nucl. Sci. Tech.* **34**, 108 (2023). <https://doi.org/10.1007/s41365-023-01256-6>

7. J. Cai, Q. Dong, Y. Han et al., An APXPS endstation for gas-solid and liquid-solid interface studies at SSRF. *Nucl. Sci. Tech.* **30**, 81 (2019). <https://doi.org/10.1007/s41365-019-0608-0>
8. J. Röhrler, *Chapter 71 X-ray absorption and emission spectra* (Elsevier, Handbook on the Physics and Chemistry of Rare Earths, 1987), pp. 453–545
9. E. Gallo, P. Glatzel, Valence to core X-ray emission spectroscopy. *Adv. Mater.* **26**, 7730–7746 (2014). <https://doi.org/10.1002/adma.201304994>
10. U. Bergmann, P. Glatzel, X-ray emission spectroscopy. *Photosynth. Res.* **102**, 255–266 (2009). <https://doi.org/10.1007/s11120-009-9483-6>
11. T. Mineva, I. Matanovic, P. Atanassov et al., Understanding active sites in pyrolyzed Fe–N–C catalysts for fuel cell cathodes by bridging density functional theory calculations and  $^{57}\text{Fe}$  Mössbauer spectroscopy. *ACS Catal.* **9**, 9359–9371 (2019). <https://doi.org/10.1021/acscatal.9b02586>
12. B.L. Geoghegan, Y. Liu, S. Peredkov et al., Combining valence-to-core X-ray emission and Cu K-edge X-ray absorption spectroscopies to experimentally assess oxidation state in organometallic Cu(I)/(II)/(III) complexes. *J. Am. Chem. Soc.* **144**, 2520–2534 (2022). <https://doi.org/10.1021/jacs.1c09505>
13. K.M. Lancaster, M. Roemelt, P. Ettenhuber et al., X-ray emission spectroscopy evidences a central carbon in the nitrogenase iron-molybdenum cofactor. *Science* **334**, 974–977 (2011). <https://doi.org/10.1126/science.1206445>
14. R. Bes, G. Leinders, K. Kvashnina, Application of multi-edge HERFD-XAS to assess the uranium valence electronic structure in potassium uranate ( $\text{KUO}_3$ ). *J. Synchrotron Radiat.* **29**, 21–29 (2022). <https://doi.org/10.1107/S1600577521012431>
15. B. Mei, C. Liu, J. Li et al., Operando HERFD-XANES and surface sensitive analyses identify the structural evolution of copper(II) phthalocyanine for electroreduction of  $\text{CO}_2$ . *J. Energy Chem.* **64**, 1–7 (2022). <https://doi.org/10.1016/j.jechem.2021.04.049>
16. D.E. Ramaker, D.C. Koningsberger, The atomic AXAFS and XANES techniques as applied to heterogeneous catalysis and electrocatalysis. *Phys. Chem. Chem. Phys.* **12**, 5514–5534 (2010). <https://doi.org/10.1039/B927120C>
17. I. Holfelder, M. Wansleben, Y. Kayser et al., A double crystal von Hamos spectrometer for traceable x-ray emission spectroscopy. *Rev. Sci. Instrum.* **92**, 123105 (2021). <https://doi.org/10.1063/5.0061183>
18. B. Mei, S. Gu, X. Du et al., A wavelength-dispersive X-ray spectrometer for in/ex situ resonant inelastic X-ray scattering studies. *X-Ray Spectrom.* **49**, 251–259 (2020). <https://doi.org/10.1002/xrs.3132>
19. J. van Bokhoven, Recent developments in X-ray absorption spectroscopy. *Phys. Chem. Chem. Phys.* **12**, 5502 (2010). <https://doi.org/10.1039/c0cp90010a>
20. X. Gao, S. Gu, Q. Gao et al., A high-resolution X-ray fluorescence spectrometer and its application at SSRF. *X-Ray Spectrom.* **42**, 502–507 (2013). <https://doi.org/10.1002/xrs.2511>
21. P. Duan, S. Gu, H. Cao et al., A three-crystal spectrometer for high-energy resolution fluorescence-detected X-ray absorption spectroscopy and X-ray emission spectroscopy at SSRF. *X-Ray Spectrom.* **46**, 12–18 (2017). <https://doi.org/10.1002/xrs.2719>
22. H. Yu, X. Wei, J. Li et al., The XAFS beamline of SSRF. *Nucl. Sci. Tech.* **26**, 050102 (2015). <https://doi.org/10.13538/j.1001-8042/nst.26.050102>
23. P. Duan, H. Bao, J. Li et al., In-situ high-energy-resolution X-ray absorption spectroscopy for  $\text{UO}_2$  oxidation at SSRF. *Nucl. Sci. Tech.* **28**, 2 (2015). <https://doi.org/10.1007/s41365-016-0155-x>
24. E. Kleymenov, J. A. van Bokhoven, C. David et al., Five-element Johann-type x-ray emission spectrometer with a single-photon-counting pixel detector. *Rev. Sci. Instrum.* **82**, 065107 (2011). <https://doi.org/10.1063/1.3600452>
25. D. Sokaras, T.-C. Weng, D. Nordlund et al., A seven-crystal Johann-type hard x-ray spectrometer at the Stanford Synchrotron Radiation Lightsource. *Rev. Sci. Instrum.* **84**, 053102 (2013). <https://doi.org/10.1063/1.4803669>
26. H. Xu, Z. Zhao, Current status and progresses of SSRF project. *Nucl. Sci. Tech.* **19**, 1–6 (2008). [https://doi.org/10.1016/S1001-8042\(08\)60013-5](https://doi.org/10.1016/S1001-8042(08)60013-5)
27. L. Tan, S. Tian, X. Liu et al., ID effects on beam dynamics in the SSRF-U storage ring. *Nucl. Sci. Tech.* **34**, 174 (2023). <https://doi.org/10.1007/s41365-023-01322-z>
28. S. Tian, G. Liu, X. Wu et al., Feedforward compensation of the insertion devices effects in the SSRF storage ring. *Nucl. Sci. Tech.* **33**, 174 (2023). <https://doi.org/10.1007/s41365-022-01052-8>
29. Z. Zhao, J. He, H. Xu et al., Continuing growth of SR science at SSRF. *Synchrotron Radiat. News* **26**, 9–15 (2013). <https://doi.org/10.1080/08940886.2013.812444>
30. M. Jiang, X. Yang, H. Xu et al., Shanghai Synchrotron Radiation Facility. *Chin. Sci. Bull.* **54**, 4171–4181 (2009). <https://doi.org/10.1007/s11434-009-0689-y>
31. Z.-H. Chen, F.-F. Sun, Y. Zou et al., Design of wide-range energy material beamline at the Shanghai synchrotron radiation facility. *Nucl. Sci. Tech.* **29**, 26 (2018). <https://doi.org/10.1007/s41365-018-0356-6>
32. L. Xie, C. Huang, Z. Liang et al., In-situ HP-STM and operando EC-STM studies of heterogeneous catalysis at interfaces. *Chin. J. Struct. Chem.* **41**, 2210029–2210044 (2022). <https://doi.org/10.14102/j.cnki.0254-5861.2022-0136>
33. H. Liu, Y. Zhou, Z. Jiang et al., QXAFS system of the BL14W1 XAFS beamline at the Shanghai Synchrotron Radiation Facility. *J. Synchrotron Rad.* **19**, 969–975 (2012). <https://doi.org/10.1107/S0909049512038873>
34. W. Zhang, J. Tang, S. Wang et al., The protein complex crystallography beamline (BL19U1) at the Shanghai Synchrotron Radiation Facility. *Nucl. Sci. Tech.* **30**, 170 (2019). <https://doi.org/10.1007/s41365-019-0683-2>
35. Y. Li, G. Liu, H. Wu et al., BL19U2: small-angle X-ray scattering beamline for biological macromolecules in solution at SSRF. *Nucl. Sci. Tech.* **31**, 117 (2020). <https://doi.org/10.1007/s41365-020-00825-3>
36. P. Glatzel, U. Bergmann, F.M.F. de Groot et al., Multiple excitations in the K fluorescence emission of Mn, Fe and Ni compounds. *AIP Conf. Proc.* **652**, 250–255 (2003). <https://doi.org/10.1063/1.1536383>
37. E.-S. Kim, Lattice design for a hybrid multi-bend achromat light source. *Nucl. Sci. Tech.* **31**, 68 (2020). <https://doi.org/10.1007/s41365-020-00774-x>
38. T.J. Penfold, C.D. Rankine, A deep neural network for valence-to-core X-ray emission spectroscopy. *Mol. Phys.* **121**, e2123406 (2023). <https://doi.org/10.1080/00268976.2022.2123406>
39. K. Bzheumikhova, J. Vinson, R. Unterumsberger et al., Titanium and titanium oxides at the K- and L-edges: comparing theoretical calculations to X-ray absorption and X-ray emission measurements. *J. Anal. At. Spectrom.* **38**, 1885–1894 (2023). <https://doi.org/10.1039/D3JA00215B>
40. S. Son, A.G. Newton, K.-N. Jo et al., Manganese speciation in Mn-rich  $\text{CaCO}_3$ : A density functional theory study. *Geochim. Cosmochim. Acta* **248**, 231–241 (2019). <https://doi.org/10.1016/j.gca.2019.01.011>
41. J. Mao, B. Mei, J. Li et al., Unraveling the dynamic structural evolution of phthalocyanine catalysts during  $\text{CO}_2$  electroreduction. *Chin. J. Struct. Chem.* **41**, 2210082–2210088 (2022). <https://doi.org/10.14102/j.cnki.0254-5861.2022-0133>

42. B. Dai, Q. Wang, J. Ma et al., XAFS study of  $\text{Cu}^{2+}$  in aqueous solution of  $\text{CuBr}_2$ . *Nucl. Sci. Tech.* **23**, 129–133 (2012). <https://doi.org/10.1016/j.nima.2012.03.020>
43. F. de Groot, G. Vankó, P. Glatzel, The 1s x-ray absorption pre-edge structures in transition metal oxides. *J. Phys. Condens. Matter* **21**, 104207 (2009). <https://doi.org/10.1088/0953-8984/21/10/104207>
44. E. Gorelov, A.A. Guda, M.A. Soldatov et al., MLFT approach with p-d hybridization for ab initio simulations of the pre-edge XANES. *Radiat. Phys. Chem.* **175**, 108105 (2020). <https://doi.org/10.1016/j.radphyschem.2018.12.025>

Springer Nature or its licensor (e.g. a society or other partner) holds exclusive rights to this article under a publishing agreement with the author(s) or other rightsholder(s); author self-archiving of the accepted manuscript version of this article is solely governed by the terms of such publishing agreement and applicable law.